Seafloor depth mapping of central Vietnam's sea area and its surrounding using gravity anomaly data and gravity geological method

Nguyen Van Sang [a], Khuong Van Long [b], Tran Tuan Dung [c], Lam Van Nguyen [d], Bui Cong Que [e], Do Van Mong [b], Bui Dang Quang [f], Ole Baltazar Andersen [g], Rene Forsberg [g], Dieu Tien Bui [h,*]

[a] *Department of Geodesy, Faculty of Geomatics and Land Administration, Hanoi University of Mining and Geology, No. 18 Pho Vien, Duc Thang, Bac Tu Liem, Hanoi 10000, Vietnam*
[b] *Vietnam's People Naval Hydrographic and Oceanographic Department, No. 3, Mac Quyet, Anh Dung, Duong Kinh, Hai Phong 04000, Vietnam*
[c] *Institute of Marine Geology and Geophysics, Vietnam Academy of Science and Technology, Building A27, No. 18, Hoang Quoc Viet, Nghia Do, Cau Giay, Hanoi 10000, Vietnam*
[d] *Department of Ocean Operations and Civil Engineering, Faculty of Engineering, Norwegian University of Science and Technology (NTNU), Larsgårdsvegen 2, 6025 Ålesund, Norway*
[e] *Institute of Geophysics, Vietnam Academy of Science and Technology, Building A8, No. 18, Hoang Quoc Viet, Nghia Do, Cau Giay, Hanoi 10000, Vietnam*
[f] *Department of Survey, Mapping and Geographic Information Vietnam, No. 2, Dang Thuy Tram Street, Co Nhue 1, Bac Tu Liem, Hanoi 10000, Vietnam*
[g] *DTU Space, Technical University of Denmark, 2800 Kgs. Lyngby, Denmark*
[h] *GIS Group, Department of Business and IT, University of South-Eastern Norway, 3800 Bø i Telemark, Norway*

Abstract

Seafloor topography mapping has a vital role in territorial management, geological investigation, natural hazard research, and marine construction; therefore, improving the accuracy of seafloor topography mapping is essential. The main objective of this research is to assess the possibility of improving the accuracy of seafloor topographic mapping for the central sea area of Vietnam and its surroundings based on the combination of satellite-derived gravity anomaly data and shipborne data. Firstly, the best satellite-derived gravity anomaly model for the study area is determined by comparing its gravity with the shipborne gravity anomaly. Then, the systematic deviation in the satellite-derived gravity anomaly is eliminated and fitted. Then, the substance density contrast (SDC) between the seabed and the seawater is derived. Subsequently, the seafloor depth was computed using the Gravity Geological method. In the next step, the computed depth is fitted with the shipborne depth to improve the accuracy and reduce the systematic deviation. The result shows that the best satellite-derived gravity anomaly model for the study area is the DTU17GRAV, with an accuracy of $\pm$ 5.06 mGal. The most suitable SDC in the study area is 1.40 g/cm^3. The final seafloor topographic map with $1' \times 1'$ grid is obtained with the root mean square deviation (RMSD) of $\pm$ 83.96 m, which is lower than that of the global terrain model of GEBCO 2022 (RMSD = $\pm$152.88 m). Therefore, it is concluded that the combination of satellite-derived gravity anomaly and shipborne data can significantly improve the accuracy of seafloor mapping for complex topographic areas. The results of this research are helpful for seabed applications and territorial management in the region.

© 2023 COSPAR. Published by Elsevier B.V. All rights reserved.

* Corresponding author.
E-mail addresses: nguyenvansang@humg.edu.vn (N.V. Sang), longdoan6@gmail.com (K.V. Long), trantuandung@yahoo.com (T.T. Dung), lam.v.nguyen@ntnu.no (L.V. Nguyen), bcque2010@gmail.com (
Bui Cong Que), dovanmong@gmail.com (D.V. Mong), dquang1979@gmail.com (B.D. Quang), oa@space.dtu.dk (O.B. Andersen), rf@space.dtu.dk (
Rene Forsberg), Dieu.T.Bui@usn.no (D. Tien Bui).

1. Introduction

Seafloor topography plays a vital role in many different fields, including tectonic studies (Haxby, Karner, LaBrecque et al., 1983) and activities of earthquakes and tsunamis (Sepúlveda, Liu and Grigoriu, 2018). In addition, maps of the seafloor topography have been considered a necessary document for extending the limits of the continental shelf of coastal countries, as stated in the United Nations Convention on the Law of the Sea (UNCLOS) (Jakobsson, Mayer and Armstrong, 2003). Besides, highly accurate seafloor topography is essential for setting up submarine cables, pipes, oil platforms, and other underwater infrastructures (Arnould, Monk, Ierodiaconou et al., 2015, Kaiser, 2020). Also, seafloor topography is essential for high-resolution tidal or ocean modeling (Gonzalez, Waldman, Sannino et al., 2023) and ocean environment research (Hildebrand and Bellefontaine, 2017). Globally, the ocean surface area covers about 362 million km^2 (Mathez and Smerdon, 2018), which accounts for approximately 71% of the earth's surface. However, only about 18% of the total seafloor topography has been mapped using shipborne depth data (Mayer et al., 2018); therefore, determining the seafloor depth with high accuracy is essential.

Literature review shows that various techniques have been introduced for measuring seafloor topography, i.e., single-beam Echosounder (SBES) (Arseni, Voiculescu, Georgescu et al., 2019), multibeam echosounder (MBES) (Calder and Mayer, 2003), satellite-derived bathymetry (SDB) (Sagawa, Yamashita, Okumura et al., 2019, Traganos, Poursanidis, Aggarwal et al., 2018), Light

Detection and Ranging (LIDAR) (Liu, Sherman and Gu, 2007), and satellite altimetry (Brêda, Paiva, Bravo et al., 2019, Yeu, Yee, Yun et al., 2018). Among these techniques, the SBES and MBES can provide high accuracy, but they are cost-consuming, especially for large areas. In addition, it is not easy to apply in ice areas (Kruss, Wiktor and Tatarek, 2019, Thomas, Lee, Coutts et al., 2022). The SDB could provide good accuracy; however, this method is preferable for shallow and clean water body areas (IHO and IOC, 2018, Pe'eri, Parrish, Azuike et al., 2014). In the case of LIDAR, this technique, which can be used together with Autonomous Surface Vehicles (ASV) and Autonomous Underwater Vehicles (UAV), has proven it's efficient for mapping at shallow or under-ice areas and high-slope seafloors (Lucieer and Forrest, 2016). On the other hand, the LIDAR measures the sea depth by determining the different times between surface water and seafloor reflection signals; therefore, it may operate ineffectively in turbidity and high-depth areas (Costa, Battista and Pittman, 2009). ASV and AUV do not require the direct appearance of engineers or ships nearby the surveying areas; however, the dependence on the power source reduces the effective operation boundary. In addition, a highly qualified engineer is required when the system has a problem. Overall, the LIDAR technique is not widely applied to determine the seafloor depth due to the limited positioning accuracy (Wölfl, Snaith, Amirebrahimi et al., 2019).

Regarding the satellite altimetry method, McKenzie and Bowin (1976) pointed out the relationship between gravity anomaly and bathymetry in the Atlantic Ocean for large areas. Then, Dixon, McNutt and Smith (1983) concluded

Table 1
Summary of the data used in this research.

No.	Data	Coverage (φ: latitude, λ: longitude)	Number of points
1	DTU10GRAV	7.5°N ≤ φ ≤ 14.5°N 109.5°E ≤ λ ≤ 115.5°E	151,200
2	DTU13GRAV	7.5°N ≤ φ ≤ 14.5°N 109.5°E ≤ λ ≤ 115.5°E	151,200
3	DTU15GRAV	7.5°N ≤ φ ≤ 14.5°N 109.5°E ≤ λ ≤ 115.5°E	151,200
4	DTU17GRAV	7.5°N ≤ φ ≤ 14.5°N 109.5°E ≤ λ ≤ 115.5°E	151,200
5	SDUST2021GRAV	7.5°N ≤ φ ≤ 14.5°N 109.5°E ≤ λ ≤ 115.5°E	151,200
6	Shipborne echo-sounding points measured in the period of 1990–1993 (having both the depth value and the gravity anomaly value)	7.5°N ≤ φ ≤ 14.5°N 109.5°E ≤ λ ≤ 115.5°E	33,313
7	Shipborne echo-sounding points measured in the period of 2009–2016 (having the depth value only)	7.5°N ≤ φ ≤ 14.5°N 109.5°E ≤ λ ≤ 115.5°E	9,403

that the altimetry satellite SEASAT could be used to derive the bathymetry. Smith and Sandwell (1994) showed that a combination of satellite altimetry and shipboard data could improve the accuracy of the bathymetry mapping. As a result, the global seafloor bathymetric model was established early in 1997 using satellite altimetry and ship-board data (Smith and Sandwell, 1997). Several bathymetric models were also successfully derived using altimetric satellite data, including DNSC08BAT, DTU10BAT, and DTU18BAT (Becker, Sandwell, Smith et al., 2009, Knudsen, Andersen, Forsberg et al., 2012). In recent research, the DTU17GRAV gravity anomaly and echo-sounder data can be combined to raise the accuracy of bathymetry in the Arctic Ocean (Abulaitijiang, Andersen and Sandwell, 2019) by employing the band-pass-filtering function (Smith and Sandwell, 1994). More recently, Tozer, Sandwell, Smith et al. (2019) pointed out that the accuracy of the global bathymetric mapping can be reached $\pm$ 150 m in the deep oceans and $\pm$ 180 m between coastlines and the continental rise with the use of satellite altimetry data (i.e., Cryosat-2, SARAL/AltiKa, and Jason-2) and shipborne data.

To derive bathymetry, a variety of studies considered the Gravity-Geologic method (GGM) to inverse bathymetry from marine gravity anomaly. This method was proposed early to determine the seafloor bathymetry from gravity anomalies on the ocean's surface because the difference in density between the ocean water and the ocean layer is insignificant (Ibrahim and Hinze, 1972, Sun, Ouyang and Guan, 2018). Crosby, McKenzie and Sclater (2006) studied the relationship between depth, age, and gravity anomalies in the Pacific Ocean. The results show that the seafloor ripples cause a gravity anomaly of about 30 mGal/km for the surrounding areas. The GGM was also considered for determining the depth in the eastern Japanese ocean area, using satellite-derived gravity anomaly and shipborne data (Kwang, Yu-Shen, Jeong et al., 2010), with a report that the GGM method is effective with a short wavelength under 12 km. The result is different when compared with the method proposed by Smith and Sandwell (1994). Therein, this method is suitable for wavelengths longer than 25 km and a density contrast of 10.25 g/cm^3.

Because the GGM only uses point-to-point data to inverse depth, not considering the basic characteristics of gravitational effect; therefore, in recent research, An, Guo, Li et al. (2022) modified the GGM into the IGGM method and applied it to a study area in the South China Sea, reporting that the accuracy at checkpoints was improved by approximately 17 m. In another research, Wei, Guo, Zhu et al. (2021) used the HY-2A/GM-derived gravity anomalies and shipborne bathymetry to predict the bathymetry over three test areas in the South China Sea with a notable conclusion that the different geological structures affect the accuracy of the GGM-based bathymetry significantly. A combination of satellite-derived gravity anomalies and shipborne data was also used to estimate the seafloor depth in the south of Alaska and the south of Greenland with good results. Herein, the difference in density contrasts was estimated using the downward continuation method (Yu-Shen, Jeong, Kwang et al., 2010). Xueshuang, Xiaoyun, Running et al. (2017) used the GGM to establish the long-wavelength gravity anomaly model for determining the bathymetry. The result demonstrated that the GGM model played a vital role in the accuracy of bathymetry estimation. Nevertheless, more research on improving the accuracy of the seafloor depth for complex areas should be carried out to have reasonable conclusions.

It is noted that although various bathymetry models, i.e., DTU10BAT (Technical University of Denmark - DTU), DTU18BAT (DTU), GEBCO 2020 (GEBCO Bathymetric Compilation Group, 2020), and GEBCO 2022 (GEBCO Bathymetric Compilation Group, 2022) are available in many areas, however, the accuracy of the seafloor depth derived from these models is still limited. Thus, how to improve the accuracy of seafloor topography mapping in complex areas, i.e., central Vietnam's Sea area and its surroundings, is still a research question. To partly fill this gap, this research aims to assess the possibility of improving the accuracy of seafloor topographic mapping for the central sea area of Vietnam and its surroundings using combined data, i.e., bathymetry data, gravity data, and satellite-derived gravity anomalies. This study area is a complex seafloor characterized by an extended continental shelf. The average depth is 500 m, and the high-slant continental slope is up to 4000 m.

2. Study area and data

2.1. Study area

The study area is located in the sea of Vietnam and its vicinity, covering an area of about 363,000 km^2, between latitudes 8°N and 14°N and longitudes 110°E and 115°E (Fig. 1). The seafloor topography is diverse and complex because this area has undergone a unique geological development process (Nguyen, 2010). The seafloor topography is more than 4000 m deep at the subsidence center, surrounded by deep-sea plains interspersed with ancient continental remnants. Deep-water troughs are considered traces of ancient subduction zones. Topographical features are characterized by continental shelves, continental slope surrounding the continental shelf with deep from around 2500 m to 3000 m, and deep depression over 4000 m (Bui and Tran, 2005).

The continental shelf is located at the western edge of the study area, with a mean depth of about 500 m. The general slope of the topographic surface is 0.1° − 0.2°, but in some places, the terrain slope is up to 5.0°, and the continental slope extends from 200 m to 4000 m (Nguyen, 2010). The outer boundary of the continental slope is where the continental crust ends and transitions into the oceanic crust. The average slope varies from a few degrees to
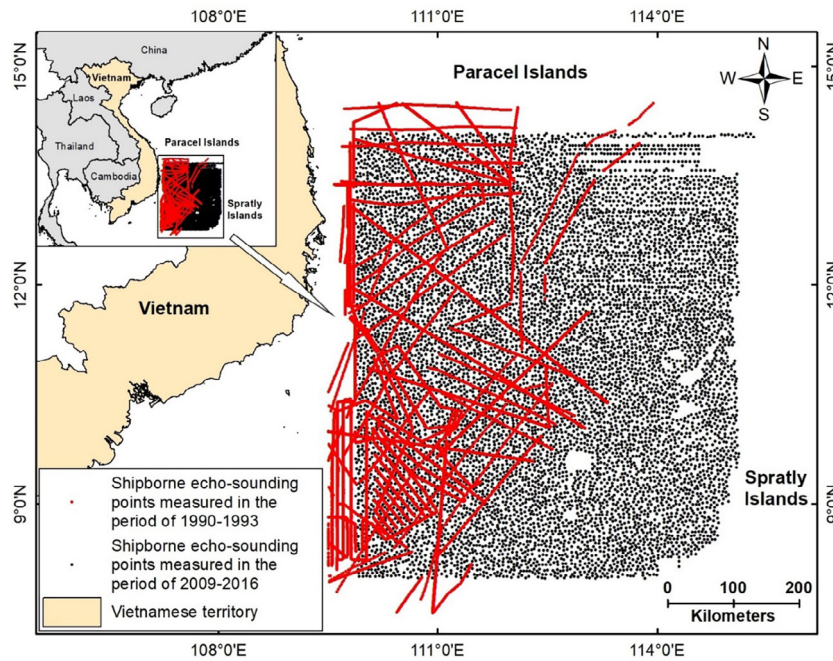
Fig. 1. Location of the study area and the shipborne echo-sounding points used.

10.0°. Most continental slopes are hills and low mountains forming a semi-plain terrain. The continental slope is formed mainly by stratigraphic structures controlled by meridian faults, buckling, and raised protrusions.

The low-lying terrain in the study area is mainly distributed at depths of over 4000 m, with the deepest reaching 4569 m (VNHOD, 2000). The process of expanding the area of the seafloor was entirely due to the activity of the spreading zone in two periods, 37 million years ago and 17 million years ago. Deep seafloor topography includes two main types: (i) Deep-sea accretion plains, distributed at a 4000 m − 5000 m, developed on the East Sea rift zone, located in the deep basin of the East Sea, expanding to the northeast and narrows to the southwest; (ii) the mountain mass remains eroded on the magmatic rock with an altitude of over 1000 m. These mountains are distributed alone on the surface of the abyssal plain, rising from the bottom of about 1000 m (Bui and Tran, 2005, Nguyen, 2010).

2.2. Data used

2.2.1. Satellite-derived gravity anomaly data

In this research, four gravity anomaly data, DTU10-GRAV, DTU13GRAV, DTU15GRAV, and DTU17-GRAV (Andersen, 2013, Andersen and Knudsen, 2014, 2016, Andersen and Knudsen, 2020) were collected (see Table 1). These data models were computed from the altimetry measurements with 1′ spacing grids and provided by the Technical University of Denmark (DTU) (available at https://ftp.space.dtu.dk/pub). The SDUST2021GRA data with a grid size of $1' \times 1'$ were also obtained (freely

available at https://zenodo.org). These data were computed using Ka-band sea surface heights (SSHs) from SARAL/AltiKA satellite and Ku-band SSHs from other satellites, including HY-2A (Zhu, Guo, Yuan et al., 2022).

2.2.2. Global seafloor depth data

In this research, four global seafloor depth models were used, DTU18BAT, GEBCO 2020, GEBCO 2022, and TOPO-V25.1. The first model with a resolution of $1' \times 1'$ was provided by the DTU, which was established using satellite-derived anomaly gravity data. Regarding the GEBCO 2020 model and the GEBCO 2022 model, the resolution is $15'' \times 15$. These models were created by the General Bathymetric Chart of the Oceans (GEBCO) using the SRTM15Plus and other data sources (Tozer, Sandwell, 2019). The last model (TOPO-V25.1) with a resolution of $1' \times 1'$ was produced by Scripps Institution of Oceanography (SIO), University of California San Diego (USA) (available at https://topex.ucsd.edu/pub/global_topo_1min).

2.2.3. Shipborne echo-sounding points measured in the period of 1990–1993

This study used 33,332 shipborne points measured using the SingleBeam Echosounder in three years, 1990, 1992, and 1993, from two projects (Que et al., 2008). The first is the scientific cooperation project between the Hanoi Institute of Oceanography (Vietnam) and the Institute of Oceanography (Russia). Accordingly, two survey trips were carried out in 1990 and 1992 using the Gagarinsky ship.

The obtained data consist of coordinates, depth, gravity anomalies, measured times, and distances of these measured points on the route. The second is the cooperation project between Vietnam and France. The Atalante ship was used to survey the East Sea in 1993. The data from the two projects above were then processed and assessed with accuracy is ± 1.0 mGal (Que, Dung and Tram, 2008). As a result, for each point, both the depth value and the gravity anomaly value were derived. Among these 33,332 shipborne points, a total of 19 points were removed due to raw error. As a result, the remaining 33,313 points (Fig. 1) were used in this research.

2.2.4. Shipborne echo-sounding points measured in the period of 2009–2016

This dataset consists of 9,403 points measured using the SingleBeam Echosounder - Simrad EA 500 in 2009 and the Multibeam Echosounder - SeaBeam 3030 and distributed between latitudes 8°N and 14°N and longitudes 110°E and 115°E (Fig. 1). Herein, the data inside the area between latitudes 12 °N and 14 °N, and longitudes 112°45′E and 115°00′E were measured using the SingleBeam Echosounder - Simrad EA 500 in 2009. The remaining areas were measured from 2010 to 2016 using the Multibeam Echosounder - SeaBeam 3030. Then, these data were processed following the IHO S44 survey standards to derive the final depth points. The coordinates of points are WGS84, whereas the depths were calculated from the mean sea level. It is important to note that the 9,403 points have the depth value only. Therefore, the gravity anomaly value for these points was further determined using the satellite-derived gravity anomaly (see Section 4.2 below).

2.2.5. Data preparation

For this research, a total of 42,716 shipborne points were used, including 33,313 points measured in the period of 1990–1993 and 9403 points measured in the period of 2009–2016 (see Table 1). After processing, these points have both depth and gravity anomaly values. For analysis, these 42,716 shipborne points were further randomly divided into three parts (Fig. 2): Part 1 consists of 14,244 points and was used to compute the seafloor depth. While Part 2 contained 14,225 points and was employed for estimating the accuracy of the depth. Whereas the remaining (Part 3) with 14,247 points was adopted for fitting the gravity-derived depth to the shipborne depth (refer to Section 3.6).

3. Methodology

The methodological flowchart for determining the seafloor depth in this research is shown in Fig. 3. The detailed steps are presented in Sections 3.1 to 3.6.

3.1. Accuracy assessment and selection of satellite-derived gravity anomaly

In this research, 151,200 points were generated for each of the DTU10GRAV, DTU13GRAV, DTU15GRAV, DTU17GRAV, and SDUST2021GRA. These points were
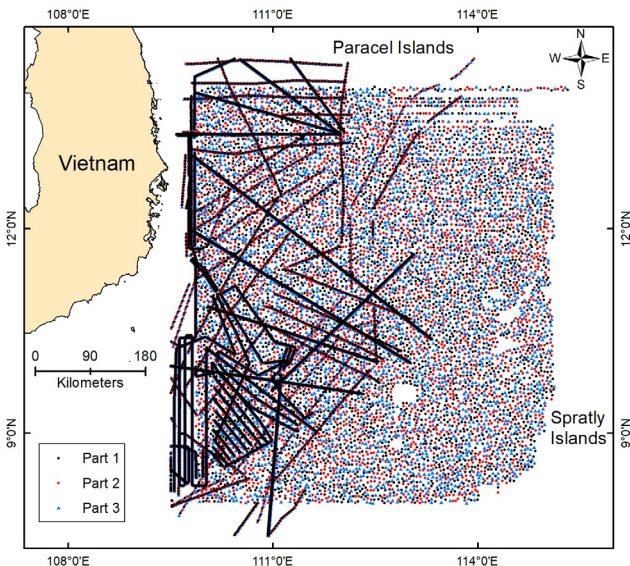

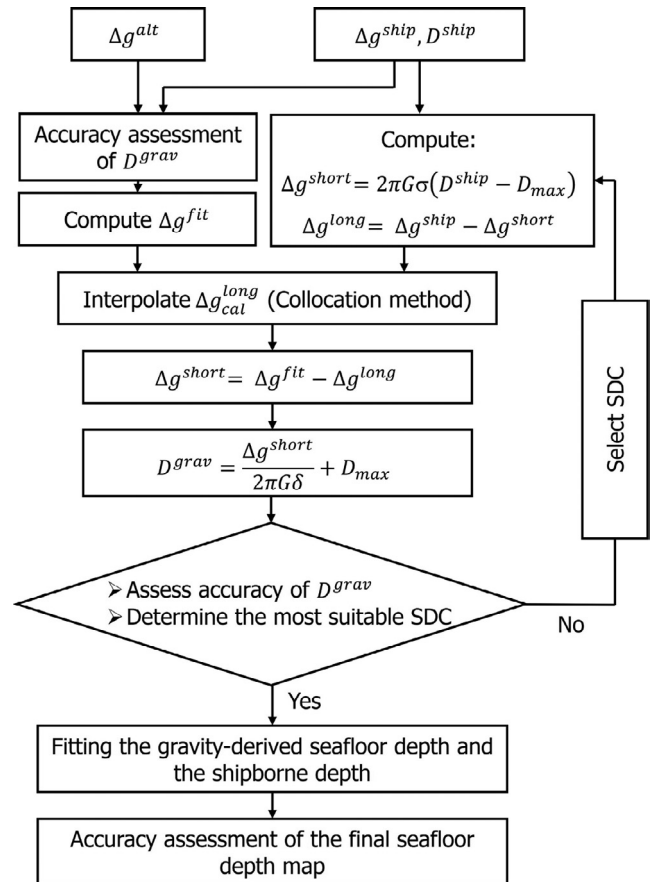Fig. 2. Shipborne data points in the study area.

Fig. 3. The methodological flowchart for determining the seafloor depth from gravity anomalies.

compared with 151,200 shipborne gravity anomaly points to assess the gravity anomaly accuracy using Eq. (1) below:

$$\delta g_i = \Delta g_i^{alt} - \Delta g_i^{ship}, i = 1, 2, \cdots, n \quad (1)$$

where n is the total of gravity points, Δg_i^{ship} and Δg_i^{alt} are the shipborne gravity anomaly and the satellite-derived gravity anomaly, respectively.

Subsequently, the mean deviation (δg_{mean}), standard deviation (*STD*), and root mean square deviation (*RMSD*) (Cohen and Sternberg, 1980) were derived using the following equations:

$$\delta g_{mean} = \frac{1}{n} \sum_{i=1}^{n} \delta g_i \quad (2)$$

$$STD = \sqrt{\frac{1}{n-1} \sum_{i=1}^{n} (\delta g_i - \delta g_{mean})^2} \quad (3)$$

$$RMSD = \sqrt{\frac{1}{n} \sum_{i=1}^{n} \delta g_i^2} \quad (4)$$

The minimun value of δg_{mean}, *STD*, and *RMSD* is the indicators to determine the best gravity anomaly model for the study area.

3.2. Satellite altimetry-derived gravity anomaly improvement

To improve the accuracy of satellite-derived gravity anomalies, the shipborne gravity anomaly points were used in two steps:

■ *Adjusting systematic deviation*: the bias system is removed by eliminating the mean difference (Eq.(2)) in the satellite-derived gravity anomaly;

■ *Fitting gravity anomalies using the Collocation method*: gravity anomaly at point P is calculated as following equations (Neiman, 2010a, Nguyen, 2012):

$$\Delta g_P^{fit} = \begin{bmatrix} C(\Delta g^{alt}, \Delta g_P) \\ C(\Delta g^{ship}, \Delta g_P) \end{bmatrix}^T$$
$$\cdot \begin{bmatrix} C(\Delta g^{alt}, \Delta g^{alt}) + C_{\Delta g^{alt}\Delta g^{alt}} & C(\Delta g^{alt}, \Delta g^{ship}) \\ C^T(\Delta g^{alt}, \Delta g^{ship}) & C(\Delta g^{ship}, \Delta g^{ship}) + C_{\Delta g^{ship}\Delta g^{ship}} \end{bmatrix}^{-1}$$
$$\cdot \begin{bmatrix} \Delta g^{alt} \\ \Delta g^{ship} \end{bmatrix} \quad (5)$$

where C is the covariance function. Other elements in Eq. (5) are as follows (Neiman, 2010a):

$$C^T(\Delta g^{alt}, \Delta g_P) = [C(\Delta g_1^{alt}, \Delta g_P) C(\Delta g_2^{alt}, \Delta g_P) \cdots C(\Delta g_k^{alt}, \Delta g_P)] \quad (6)$$

$$C^T(\Delta g^{ship}, \Delta g_P) = [C(\Delta g_1^{ship}, \Delta g_P) C(\Delta g_2^{ship}, \Delta g_P) \cdots C(\Delta g_m^{ship}, \Delta g_P)] \quad (7)$$

$$C(\Delta g^{alt}, \Delta g^{alt})$$
$$= \begin{bmatrix} C(\Delta g_1^{alt}, \Delta g_1^{alt}) C(\Delta g_1^{alt}, \Delta g_2^{alt}) \cdots C(\Delta g_1^{alt}, \Delta g_k^{alt}) \\ C(\Delta g_2^{alt}, \Delta g_1^{alt}) C(\Delta g_2^{alt}, \Delta g_2^{alt}) \cdots C(\Delta g_2^{alt}, \Delta g_k^{alt}) \\ \cdots \\ C(\Delta g_k^{alt}, \Delta g_1^{alt}) C(\Delta g_k^{alt}, \Delta g_2^{alt}) \cdots C(\Delta g_k^{alt}, \Delta g_k^{alt}) \end{bmatrix} \quad (8)$$

$$C(\Delta g^{ship}, \Delta g^{ship})$$
$$= \begin{bmatrix} C(\Delta g_1^{ship}, \Delta g_1^{ship}) C(\Delta g_1^{ship}, \Delta g_1^{ship}) \cdots C(\Delta g_1^{ship}, \Delta g_m^{ship}) \\ C(\Delta g_2^{ship}, \Delta g_1^{ship}) C(\Delta g_2^{ship}, \Delta g_2^{ship}) \cdots C(\Delta g_2^{ship}, \Delta g_m^{ship}) \\ \cdots \\ C(\Delta g_k^{ship}, \Delta g_1^{ship}) C(\Delta g_k^{ship}, \Delta g_2^{ship}) \cdots C(\Delta g_k^{ship}, \Delta g_m^{ship}) \end{bmatrix} \quad (9)$$

$$C(\Delta g^{alt}, \Delta g^{ship})$$
$$= \begin{bmatrix} C(\Delta g_1^{alt}, \Delta g_1^{ship}) C(\Delta g_1^{alt}, \Delta g_2^{ship}) \cdots C(\Delta g_1^{alt}, \Delta g_k^{ship}) \\ C(\Delta g_2^{alt}, \Delta g_1^{ship}) C(\Delta g_2^{alt}, \Delta g_2^{ship}) \cdots C(\Delta g_2^{alt}, \Delta g_k^{ship}) \\ \cdots \\ C(\Delta g_k^{alt}, \Delta g_1^{ship}) C(\Delta g_k^{alt}, \Delta g_2^{ship}) \cdots C(\Delta g_k^{alt}, \Delta g_m^{ship}) \end{bmatrix} \quad (10)$$

$$C_{\Delta g^{alt}\Delta g^{alt}}$$
$$= \begin{bmatrix} C_{\Delta g_1^{alt}\Delta g_1^{alt}} C_{\Delta g_1^{alt}\Delta g_2^{alt}} \cdots C_{\Delta g_1^{alt}\Delta g_k^{alt}} \\ C_{\Delta g_2^{alt}\Delta g_1^{alt}} C_{\Delta g_2^{alt}\Delta g_2^{alt}} \cdots C_{\Delta g_2^{alt}\Delta g_k^{alt}} \\ \cdots \\ C_{\Delta g_k^{alt}\Delta g_1^{alt}} C_{\Delta g_k^{alt}\Delta g_2^{alt}} \cdots C_{\Delta g_k^{alt}\Delta g_k^{alt}} \end{bmatrix} \quad (11)$$

$$C_{\Delta g^{ship}\Delta g^{ship}}$$
$$= \begin{bmatrix} C_{\Delta g_1^{ship}\Delta g_1^{ship}} C_{\Delta g_1^{ship}\Delta g_2^{ship}} \cdots C_{\Delta g_1^{ship}\Delta g_m^{ship}} \\ C_{\Delta g_2^{ship}\Delta g_1^{ship}} C_{\Delta g_2^{ship}\Delta g_2^{ship}} \cdots C_{\Delta g_2^{ship}\Delta g_m^{ship}} \\ \cdots \\ C_{\Delta g_m^{ship}\Delta g_1^{ship}} C_{\Delta g_m^{ship}\Delta g_2^{ship}} \cdots C_{\Delta g_m^{ship}\Delta g_m^{ship}} \end{bmatrix} \quad (12)$$

The matrix calculated in Eq.(1) is diagonal if covariance values between points are not considered. The covariance between point j and point k is calculated as follows (Forsberg, 1987):

$$C_{j,k}(s) = -f \sum_{i=0}^{3} \alpha_i log(D_i + r_i) \quad (13)$$

$$\begin{cases} r_i = \sqrt{s^2 + D_i^2} \\ D_i = D + i \times T \\ \alpha_0 = -\alpha_3 = 1 \\ \alpha_1 = -\alpha_2 = -3 \\ f = \frac{C_0}{log\left(\frac{D_1^3 D_3}{D_0 D_2^3}\right)} \end{cases} \quad (14)$$

where s is the distance between points j and k; whereas C_0, D, and T are defined using an approximation of vari-
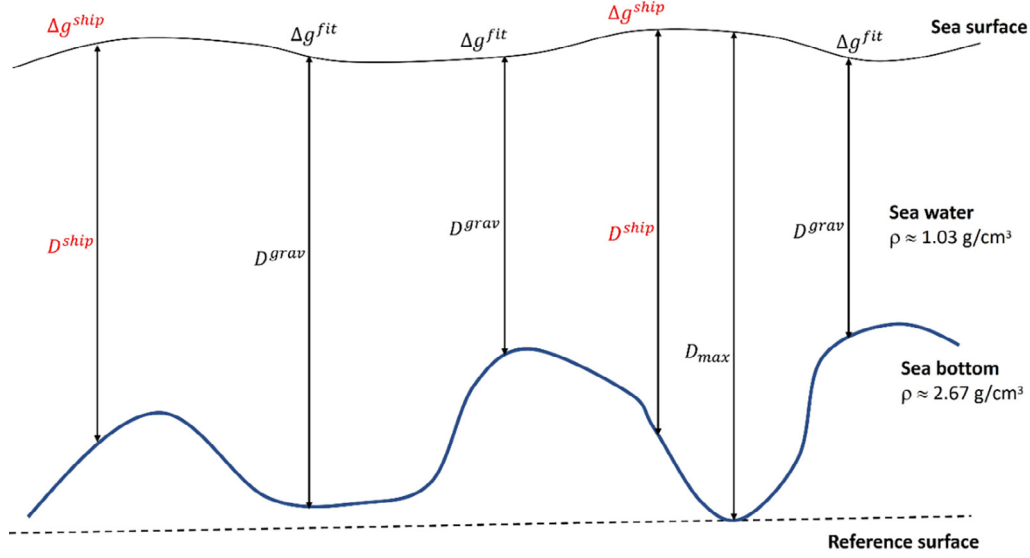
Fig. 4. Seafloor determination from the gravity anomaly in this research.

ance and empirical covariance with theoretical covariance in Eq.(13).

3.3. Calculation of seafloor depth using the Gravity-Geologic method

Based on the Gravity-Geologic (GG) method, the gravity anomaly (Δg) is divided into two small parts: (i) the short-wavelength gravity anomaly part (Δg^{short}) which depended on the variations of local bedrock topography, and (ii) the long-wavelength gravity anomaly part (Δg^{long}) generated using the deeper mass variations (Ibrahim and Hinze, 1972, Kwang, Yu-Shen, 2010, Xueshuang, Xiaoyun, 2017, Yu-Shen, Jeong, 2010). Explanation of short-wavelength gravity and long-wavelength gravity can be found in (Kostoglodov, Kogan and Magnitskaya, 1981, Phillips and Lambeck, 1980, Xiang, Wan, Zhang et al., 2017).

The short-wavelength gravity anomaly for the points that have available gravity anomaly and depth (Ibrahim and Hinze, 1972, Kwang, Yu-Shen, 2010) is shown below:

$$\Delta g^{short} = 2\pi G \sigma (D^{ship} - D_{max}) \tag{15}$$

where G is the gravitational constant (G = 6.672 × 10⁻⁸ cm³/gs²), σ is the SDC between seawater and seafloor, D^{ship} and D_{max} are the shipborne depth and maximum depth in the study area, respectively (Fig. 4).

The long-wavelength gravity anomaly is calculated using Eq.(16) (Kwang, Yu-Shen, 2010, Yu-Shen, Jeong, 2010) as follows:

$$\Delta g^{long} = \Delta g^{ship} - \Delta g^{short} \tag{16}$$

At these points, which have only the gravity anomalies, the long-wavelength gravity anomaly is interpolated from available points (Δg^{long}). The short-wavelength gravity

anomaly-derived depth (D^{grav}) can be calculated using Eqs. (17) and (18) (Kwang, Yu-Shen, 2010, Yu-Shen, Jeong, 2010) as:

$$\Delta g^{short} = \Delta g^{fit} - \Delta g^{long} \tag{17}$$

$$D^{grav} = \frac{\Delta g^{short}}{2\pi G \sigma} + D_{max} \tag{18}$$

Eq.(16) shows that the calculation of Δg^{short} and σ is the core steps for determining the seafloor depth using the GG method.

3.4. Interpolation of long-wavelength gravity anomaly implementing the Collocation method

The long-wavelength gravity anomaly at specific point P is computed using the Collocation method (Neiman, 2010a) below:

$$\Delta g_P^{long} = C^T \left(\Delta g^{long}, \Delta g_P^{long} \right) . \left[C \left(\Delta g^{long}, \Delta g^{long} \right) + C_\Delta \right]^{-1} . \Delta g^{long} \tag{19}$$

where C and Δg^{long} are covariance function and available long-wavelength gravity anomaly matrix, respectively. The variance and covariance values are calculated using Eqs. (13) and (14) in Section 3.2.

3.5. Determination of suitable substance density contrast

Determining the suitable SDC is essential for implementing the GG method (Kim, Hsiao, Kim et al., 2010), and this is an iterative process. The difference between the calculated seafloor depth and the shipborne-derived depth (δD) is derived using Eq. (20) below:

$$\delta D_i = D_i^{grav} - D_i^{ship}, i = 1, 2, \cdots n \tag{20}$$

The best SDC for the study area is selected based on the mean difference (δD_{mean}), standard deviation (STD_D), root mean square deviation ($RMSD_D$), and the Pearson correlation coefficient (r) between calculated and measured depth as formulas (Adler and Parmryd, 2010, Cohen and Sternberg, 1980). Herein, the best SDC characterizes by the δD_{mean}, STD_D, $RMSD_D$ are smallest, whereas r is largest.

$$\delta D_{mean} = \frac{1}{n}\sum_{i=1}^{n}\delta D_i \qquad (21)$$

$$STD_D = \sqrt{\frac{1}{n-1}\sum_{i=1}^{n}\left(\delta D_i - \delta D_{mean}\right)^2} \qquad (22)$$

$$RMSD_D = \sqrt{\frac{1}{n}\sum_{i=1}^{n}\delta D_i^2} \qquad (23)$$

$$r = \frac{\sum_{i=1}^{m}\left(D_i^{ship} - D_{mean}^{ship}\right)\cdot\left(D_i^{grav} - D_{mean}^{grav}\right)}{\sqrt{\sum_{i=1}^{m}\left(D_i^{ship} - D_{mean}^{ship}\right)^2 \cdot \sum_{i=1}^{m}\left(D_i^{grav} - D_{mean}^{grav}\right)^2}} \qquad (24)$$

where D_{mean}^{ship} and D_{mean}^{grav} are the mean measured depth and the mean depth.

3.6. Unification of calculated seafloor depth and direct echo soundings

The differences between the measured depth and the gravity anomaly-derived depth include the systematic bias and the stochastic element. The systematic bias was eliminated by removing the mean values, whereas the stochastic elements were fitted by using the Collocation method.

Assume that k and m were numbers of gravity anomaly-calculated depths $D_1^{grav}, D_2^{grav}, ..., D_k^{grav}$ and measured depths $D_1^{ship}, D_2^{ship}, ..., D_m^{ship}$, respectively. The short formula for the depth determination at point P is shown in Eq.(25) (Neiman, 2010a, Nguyen, 2013):

$$D_P^{fit} = C_D^T(C_D + C_\Delta)^{-1}D \qquad (25)$$

The full description of Eq.(25) can be rewritten as follows:

$$D_P^{fit} = \begin{bmatrix} C(D^{grav}, D_P) \\ C(D^{ship}, D_P) \end{bmatrix}^T$$
$$\cdot \begin{bmatrix} C(D^{grav}, D^{grav}) + C_{D^{grav}D^{grav}} & C(D^{grav}, D^{ship}) \\ C^T(D^{grav}, D^{ship}) & C(D^{ship}, D^{ship}) + C_{D^{ship}D^{ship}} \end{bmatrix}^{-1}$$
$$\cdot \begin{bmatrix} D^{grav} \\ D^{ship} \end{bmatrix} \qquad (26)$$

where:

$$C^T(D^{grav}, D_P) = [C(D_1^{grav}, D_P)C(D_2^{grav}, D_P)\cdots C(D_k^{grav}, D_P)] \qquad (27)$$

$$C^T(D^{ship}, D_P) = [C(D_1^{ship}, D_P)C(D_2^{ship}, D_P)\cdots C(D_m^{ship}, D_P)] \qquad (28)$$

$$C(D^{grav}, D^{grav})$$
$$= \begin{bmatrix} C(D_1^{grav}, D_1^{grav})C(D_1^{grav}, D_2^{grav})\cdots C(D_1^{grav}, D_k^{grav}) \\ C(D_2^{grav}, D_1^{grav})C(D_2^{grav}, D_2^{grav})\cdots C(D_2^{grav}, D_k^{grav}) \\ \cdots \\ C(D_k^{grav}, D_1^{grav})C(D_k^{grav}, D_2^{grav})\cdots C(D_k^{grav}, D_k^{grav}) \end{bmatrix} \qquad (29)$$

$$C(D^{ship}, D^{ship})$$
$$= \begin{bmatrix} C(D_1^{ship}, D_1^{ship})C(D_1^{ship}, D_2^{ship})\cdots C(D_1^{ship}, D_m^{ship}) \\ C(D_2^{ship}, D_1^{ship})C(D_2^{ship}, D_2^{ship})\cdots C(D_2^{ship}, D_m^{ship}) \\ \cdots \\ C(D_m^{ship}, D_1^{ship})C(D_m^{ship}, D_2^{ship})\cdots C(D_m^{ship}, D_m^{ship}) \end{bmatrix} \qquad (30)$$

$$C(D^{grav}, D^{ship})$$
$$= \begin{bmatrix} C(D_1^{grav}, D_1^{ship})C(D_1^{grav}, D_2^{ship})\cdots C(D_1^{grav}, D_k^{ship}) \\ C(D_2^{grav}, D_1^{ship})C(D_2^{grav}, D_2^{ship})\cdots C(D_2^{grav}, D_k^{ship}) \\ \cdots \\ C(D_m^{grav}, D_1^{ship})C(D_m^{grav}, D_2^{ship})\cdots C(D_m^{grav}, D_k^{ship}) \end{bmatrix} \qquad (31)$$

$$C_{D^{grav}D^{grav}}$$
$$= \begin{bmatrix} C_{D_1^{grav}D_1^{grav}} C_{D_1^{grav}D_2^{grav}} \cdots C_{D_1^{grav}D_k^{grav}} \\ C_{D_2^{grav}D_2^{grav}} C_{D_2^{grav}D_2^{grav}} \cdots C_{D_2^{grav}D_k^{grav}} \\ \cdots \\ C_{D_k^{grav}D_1^{grav}} C_{D_k^{grav}D_2^{grav}} \cdots C_{D_k^{grav}D_k^{grav}} \end{bmatrix} \qquad (32)$$

Table 2
Comparison of the satellite-derived gravity anomaly and the shipborne gravity anomaly.

No.	Model	δg_{max} (mGal)	δg_{min} (mGal)	δg_{mean} (mGal)	STD (mGal)	RMSD (mGal)
1	DTU10GRAV	54.27	−34.42	2.67	± 5.90	± 6.48
2	DTU13GRAV	54.92	−34.10	2.63	± 5.82	± 6.38
3	DTU15GRAV	57.43	−32.26	2.72	± 5.66	± 6.28
4	DTU17GRAV	56.07	−33.38	2.70	± 5.60	± 6.22
5	SDUST2021GRAV	59.16	−31.17	2.66	± 5.68	± 6.27

$$C_{D^{ship}D^{ship}} = \begin{bmatrix} C_{D_1^{ship}D_1^{ship}} C_{D_1^{ship}D_2^{ship}} \cdots C_{D_1^{ship}D_m^{ship}} \\ C_{D_2^{ship}D_1^{ship}} C_{D_2^{ship}D_2^{ship}} \cdots C_{D_2^{ship}D_m^{ship}} \\ \cdots \\ C_{D_m^{ship}D_1^{ship}} C_{D_m^{ship}D_2^{ship}} \cdots C_{D_m^{ship}D_m^{ship}} \end{bmatrix} \quad (33)$$

The variance and covariance values can be calculated in Eqs. (13) and (14) in section 3.2 for the depth.

4. Results and analysis

4.1. Accuracy assessment of the satellite-derived gravity anomaly data

To assess the accuracy of the gravity anomaly from the five satellite-derived gravity anomaly models, DTU10-GRAV, DTU13GRAV, DTU15GRAV, DTU17GRAV, and SDUST2021GRAV, a total of 13,713 shipborne gravity anomaly points were used. These points were randomly selected from the 33,313 shipborne gravity anomaly points mentioned in Section 2.2.3. The result is shown in Table 2.

The results show that δg_{mean} is from -34.42 mGal to -34.10 mGal, indicating that there is a systematic deviation between the satellite-derived gravity anomalies and the shipborne-derived gravity anomalies. Among them, the DTU17GRAV model provides the highest accuracy results. The STD and RMSD are $\pm$ 6.22 mGal and $\pm$ 5.60 mGal, respectively. Therefore, this DTU17-GRA model is selected for the following computational steps.

4.2. Improvement of the satellite-derived gravity anomaly by fitting with the shipborne gravity anomaly

In this step, 13,713 shipborne gravity anomaly points are randomly divided into two parts (Fig. 5): the first one containing 12,648 points (approximately 90.0 %) was used for fitting with the DTU17GRAV model, and the second one consisting of the remaining (1,065 points, about 10.0 %) was used for validating the result.

The fitting process was implemented using the GPFit and GPCol1 functions in the Gravsoft program (Forsberg and Tscherning, 2008). The result is shown in Fig. 6 and Table 3.

The result shows that the RMSD of the DTU17GRAV reduces from $\pm$ 7.25 mGal before the fitting gravity anomaly to $\pm$ 5.06 mGal after the fitting gravity anomaly, whereas the Mean of the DTU17GRAV decreases from $+$ 4.98 mGal before the fitting to $+$ 0.28 mGal after the fitting. These indicate that a significant improvement is obtained regarding the accuracy of the satellite-derived gravity anomaly from DTU17GRAV.

4.3. Result of the suitable density contrast

Theoretically, it is assumed that the SDC is roughly 1.64 g/cm^3, which is the mean density difference between
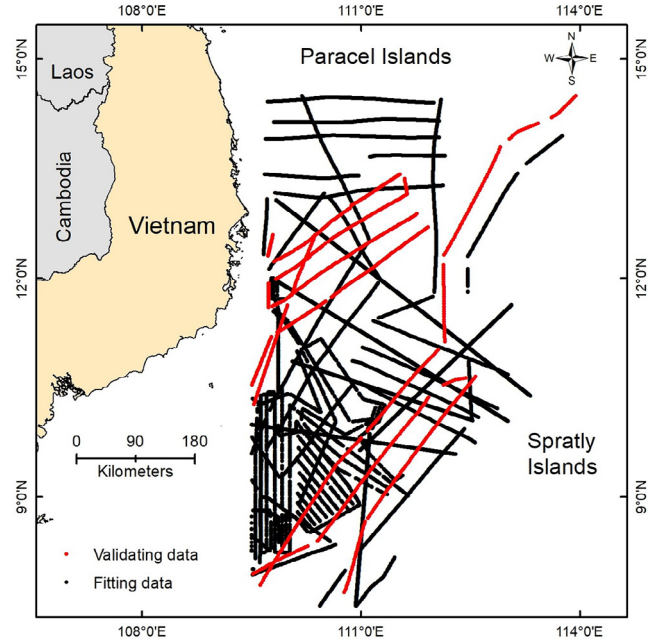

Fig. 5. Distribution of the fitting and the validating points in this research.
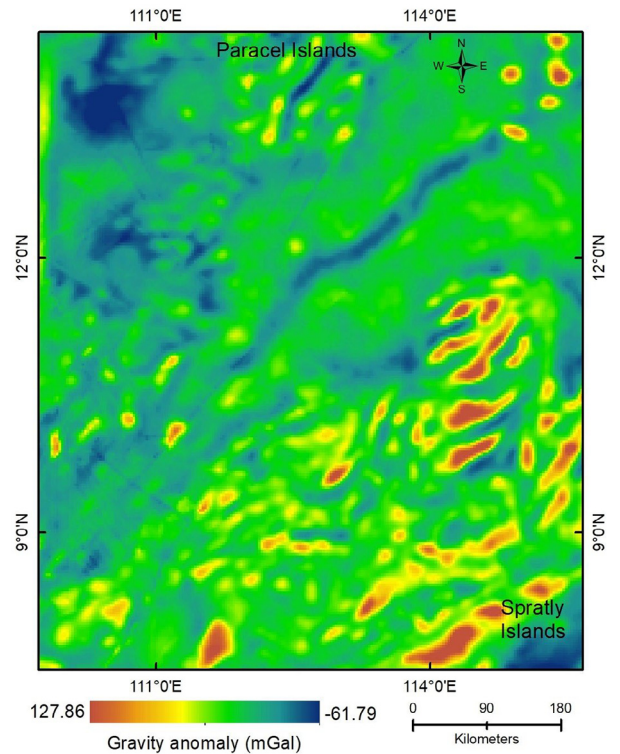

Fig. 6. The fitted gravity anomaly map for the study area.

Table 3
Statistics of the DTU17GRAV gravity anomaly before the fitting gravity anomaly and after the fitting gravity anomaly (in mGal).

No	DTU17GRAV	Max	Min	Mean	STD	RMSD
1	Before the fitting	23.98	−9.08	4.98	± 5.28	± 7.25
2	After the fitting	19.66	−14.34	0.28	± 5.05	± 5.06

the bedrock (2.67 g/cm^3) and the seawater (1.03 g/cm^3). However, the SDC is varied across the local geology areas. Therefore, to find a suitable SDC value for the study area, we tested SDC from 1.10 g/cm^3 and 3.00 g/cm^3. The selection of the value for each step mainly depends on the result of the previous step, with the target being to minimize the RMSD value and maximize the r values. The result is shown in Table 4 and Fig. 7. Based on the computed results, the SDC value of 1.40 g/cm^3 is the best value for the study area, which minimized the error (RMSD = ±85.54 m) and maximized the Pearson correlation coefficient (r = 0.997).

4.4. Determination of the seafloor depth from the gravity anomaly corresponding to the most appropriate SDC

4.4.1. Computation of long-wavelength gravity anomaly

Using the SDC value of 1.40 g/cm^3 in the previous step, the long-wavelength gravity anomalies at the shipborne points were obtained (Fig. 8). Their maximum, minimum, and average values for the study area were + 7.50 mGal, −269.30 mGal, and −166.40 mGal, respectively.

4.4.2. Calculation of the seafloor depth using the gravity anomaly

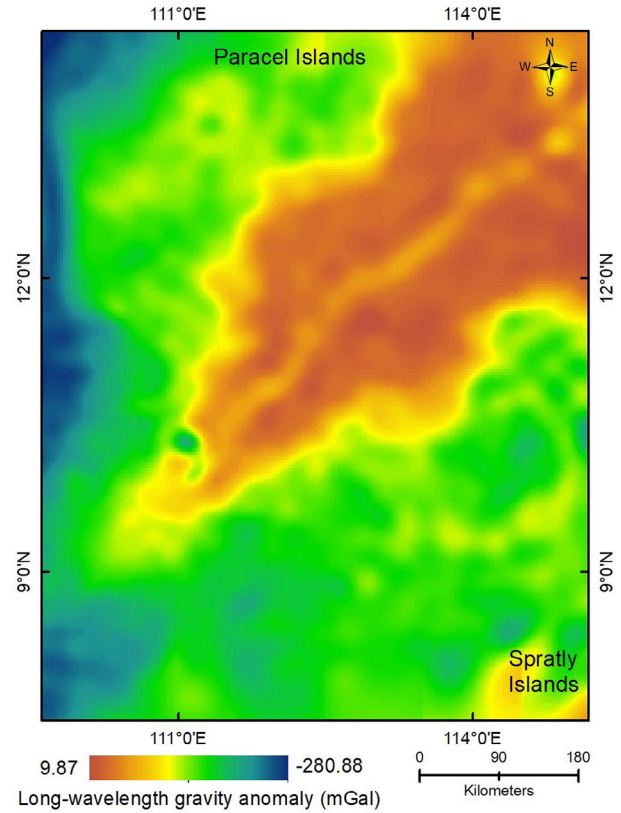Fig. 9 shows the seafloor depth map computed from the gravity anomaly in the study area. This map was obtained

Fig. 8. The map of long-wavelength gravity anomaly in the study area.

Table 4
Comparison of the calculated depths based on the SDC difference.

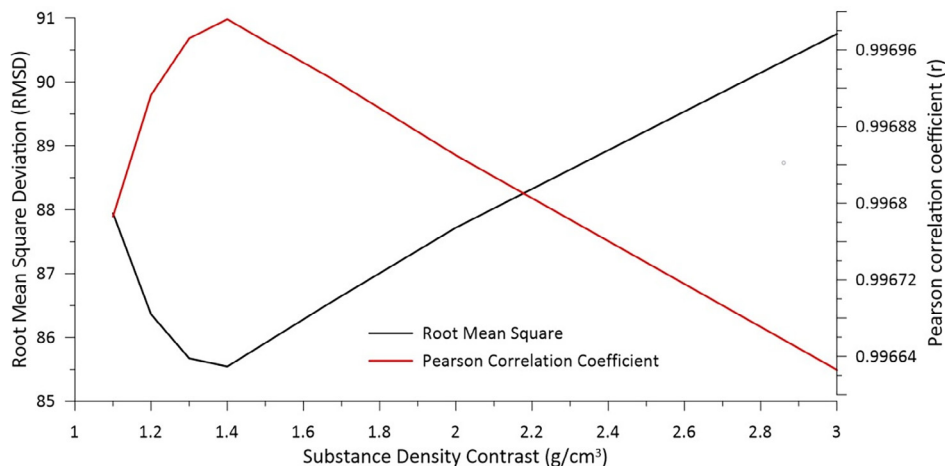| No.	SDC (g/cm^3)	Max (m)	Min (m)	Mean (m)	RMSD (m)	STD (m)	r
1	1.10	849.28	−913.69	−1.46	± 87.94	± 87.93	0.997
2	1.20	887.22	−931.70	−1.35	± 86.36	± 86.35	0.997
3	1.30	918.81	−948.45	−1.26	± 85.67	± 85.66	0.997
4	**1.40**	**944.29**	**−964.04**	**−1.18**	**± 85.54**	**± 85.54**	**0.997**
5	1.50	964.90	−972.93	−1.13	± 85.91	± 85.91	0.997
6	1.67	1012.90	−991.93	−1.05	± 86.54	± 86.54	0.997
7	2.00	1075.14	−1023.70	−0.96	± 87.72	± 87.71	0.997
8	3.00	1148.49	−1136.98	−0.87	± 90.75	± 90.75	0.997

Fig. 7. The dependence of SDC on RMSD and r.
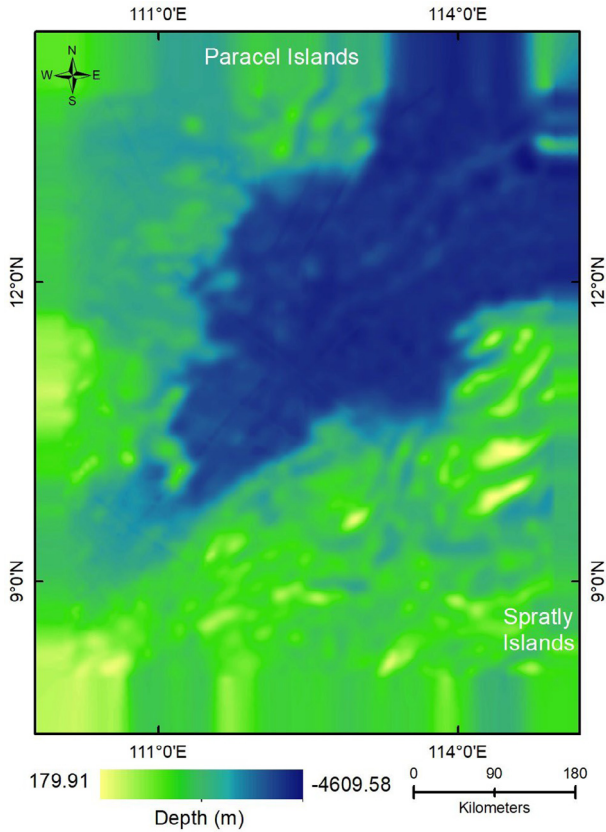
Fig. 9. The gravity-derived seafloor depth map calculated from the gravity anomaly.

from 107,341 points. The maximum, minimum, and average values of this map were 211.68 m, −4613.78 m, and −2708.85 m, respectively. It could be seen that these points with positive depth values belong to Paracel Islands and Spratly Islands.

4.4.3. Comparison of the gravity-derived seafloor depth with the shipborne depth

It could be seen that, after fitting gravity, RMSD of the gravity-derived seafloor depth reduced from ± 119.74 m to ± 85.54 m, and Mean decreased from 33.12 m to

−1.18 m, indicating that the accuracy of the gravity-derived seafloor depth has improved significantly with the use of the shipborne gravity points.

In order to check if the deviation between the gravity-derived seafloor depths and the shipborne depths is statistically random, an analysis is carried out on the correlation between the number of the gravity-derived seafloor depth points where the DV is less than RMSD. It is noted that the DV is computed using Eq. (20). The result is shown in Table 6.

It could be seen that 83.78 % of the points have DV less than 1-time RMSD, whereas the percentage of the points increases to 98.00 % when 3-time RMSD is considered. In contrast, only 47 points (0.33%) have DV larger than 500 m (Table 6). These indicate that the DV is statistical randomness.

Fig. 10 shows the distribution of DV in the study area. It could be seen that the distribution of DV follows the normal distribution rule (Fig. 10a) and a high correlation between the computed depth and the shipborne depth (Fig. 10b).

In order to show the location of these points regarding the DV magnitude, a 3D map was further compiled (Fig. 11). It can be observed that the points with high DV are mainly in areas of complex topography and around the Spratly Islands. Besides, the DV decreases significantly after the fitting (Fig. 11b).

4.5. Unification of the gravity-derived seafloor depth and the shipborne depth

4.5.1. Fitting the gravity-derived seafloor depth and the shipborne depth

The gravity-derived seafloor depth points were fitted with the 14,247 shipborne depth points (Part 3 in Section 2.2.5) as follows:

■ *Step 1 - Systematic deviation adjusting.* The gravity-derived seafloor depth of these points was adjusted via the mean value of −1.18 m (Table 5);
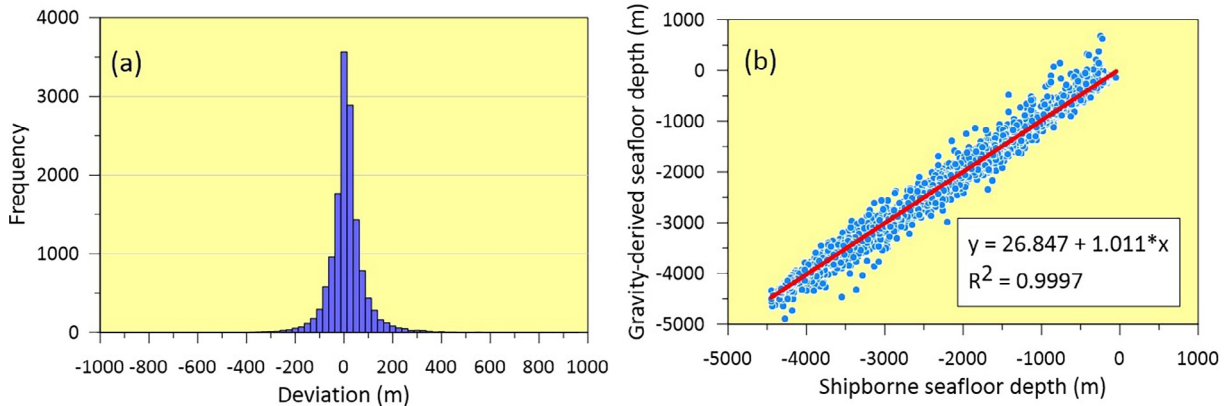

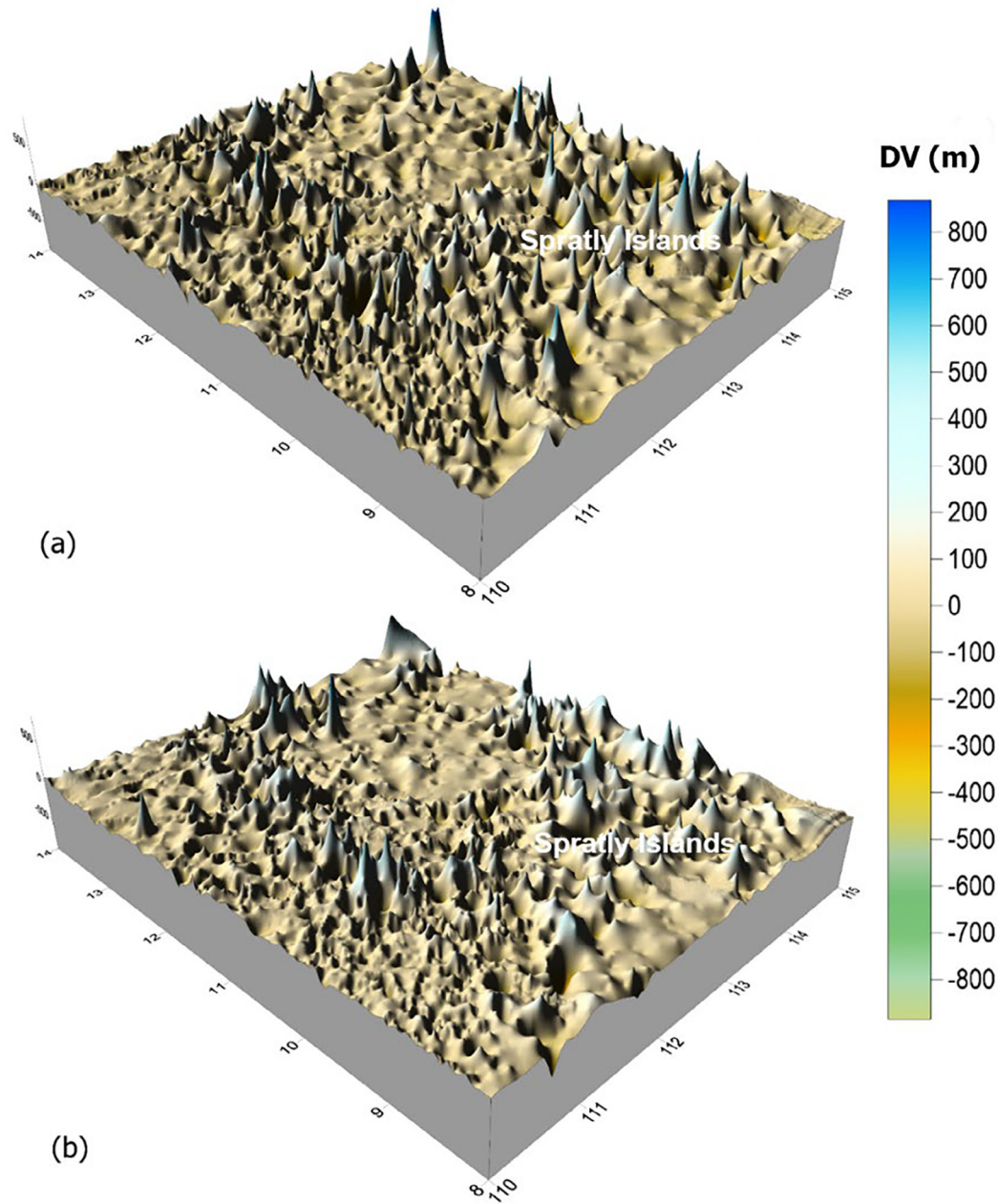Fig. 10. The map of DVs' distribution (a) and DVs' correlation (b).

Fig. 11. Distribution of the gravity-derived seafloor depth point with their DV: (a) before and (b) after the fitting depth.

Table 5
The difference between the gravity-derived seafloor depth (m) and the shipborne depth (m).

No.	Gravity-derived seafloor depth	Max	Min	Mean	RMSD	STD
1	Before the fitting gravity anomaly	1197.72	−1061.19	33.13	± 119.74	± 115.06
2	After the fitting gravity anomaly	944.29	−964.04	−1.18	± 85.54	± 85.55

■ *Step 2 - Random deviation fitting*. After removing the systematic deviation, the gravity-derived seafloor depths were fitted with the shipborne depths using the Collocation method. Because the Collocation method requires the mean value of the depth to be zero, we removed the mean depth before the fitting, and then, after the fitting, the mean depth was restored (Fig. 12). And then, the final seafloor depth map was obtained.

Table 6
DV of the gravity-derived seafloor depth point versus RMSD.

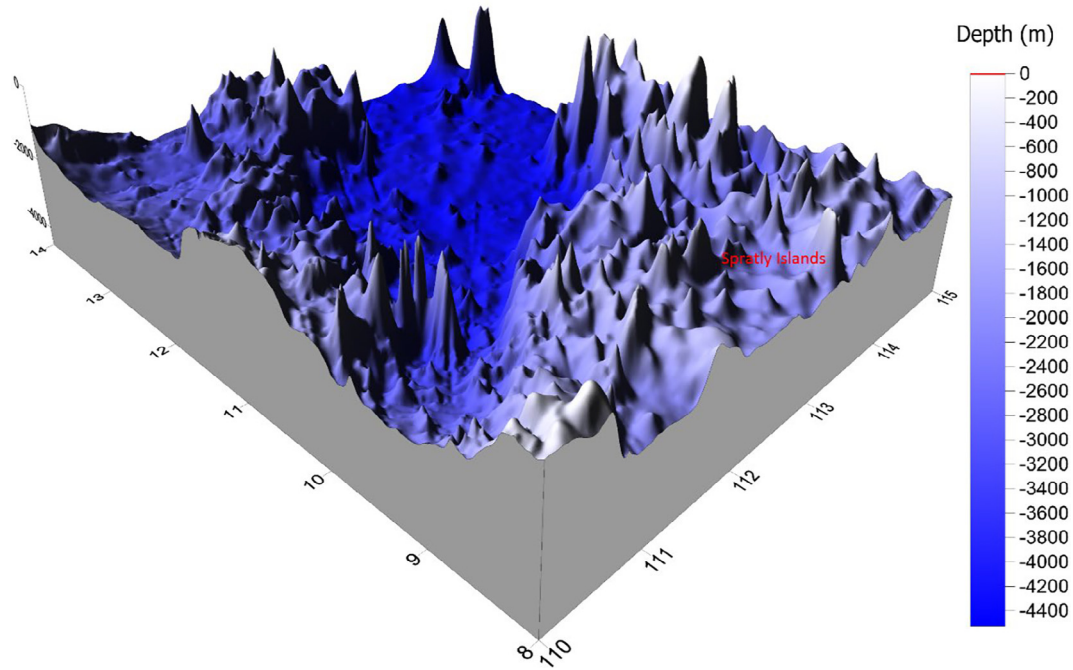| No.	Number of points	Percentage (%)	DV (m)
1	11,917	83.78	$-RMSD < DV < RMSD$
2	13,544	95.21	$-2 \times RMSD < DV < 2 \times RMSD$
3	13,940	98.00	$-3 \times RMSD < DV < 3 \times RMSD$
4	47	0.33	$DV < -500$ or $DV > 500$

Fig. 12. The 3D map of the final seafloor depth of the study area.

Table 7
The difference between the shipborne depth and the seafloor depth before and after the fitting depth (the final seafloor depth).

Model	Max (m)	Min (m)	Mean (m)	RMSD (m)	STD (m)	r
Before the fitting depth	944.29	−964.04	−1.18	± 85.54	± 85.54	0.997
After the fitting depth (the final seafloor depth)	**877.81**	**−958.93**	**0.73**	**± 83.96**	**± 83.95**	**0.997**
DTU18BAT	2009.85	−3344.26	−10.92	± 210.22	± 209.94	0.982
GEBCO 2020	2208.10	−3496.83	−9.02	± 187.99	± 187.78	0.986
GEBCO 2022	2166.09	−1815.86	−4.46	± 152.88	± 152.82	0.991
TOPO-V25.1	1911.45	−1772.79	−2.61	± 157.46	± 157.44	0.990

4.5.2. Comparison of the final seafloor depth map to the shipborne depth

In order to assess the accuracy, the final seafloor depth map was compared to the 14,225 shipborne depth points (in Part 2 in Section 2.2.5). The difference between the shipborne depth and the seafloor depth before and after the fitting depth is shown in Table 7.

The results in Table 7 indicate that the depth's relative accuracy (the accuracy divided by the depth) increased by 1.84%, and the RMSD reduced from ± 85.54 m to ± 83.

94 m. Besides, all absolute maximum, minimum, and mean values are reduced, and the Pearson correlation coefficient increases.

4.5.3. Comparison of the global depth models with the shipborne depth

In this research, the depth from the four global models (DTU18BAT, GEBCO 2020, GEBCO 2022, and TOPO-V25.1) was further compared with the shipborne depth points. The result is shown in Table 7 and Fig. 13. The
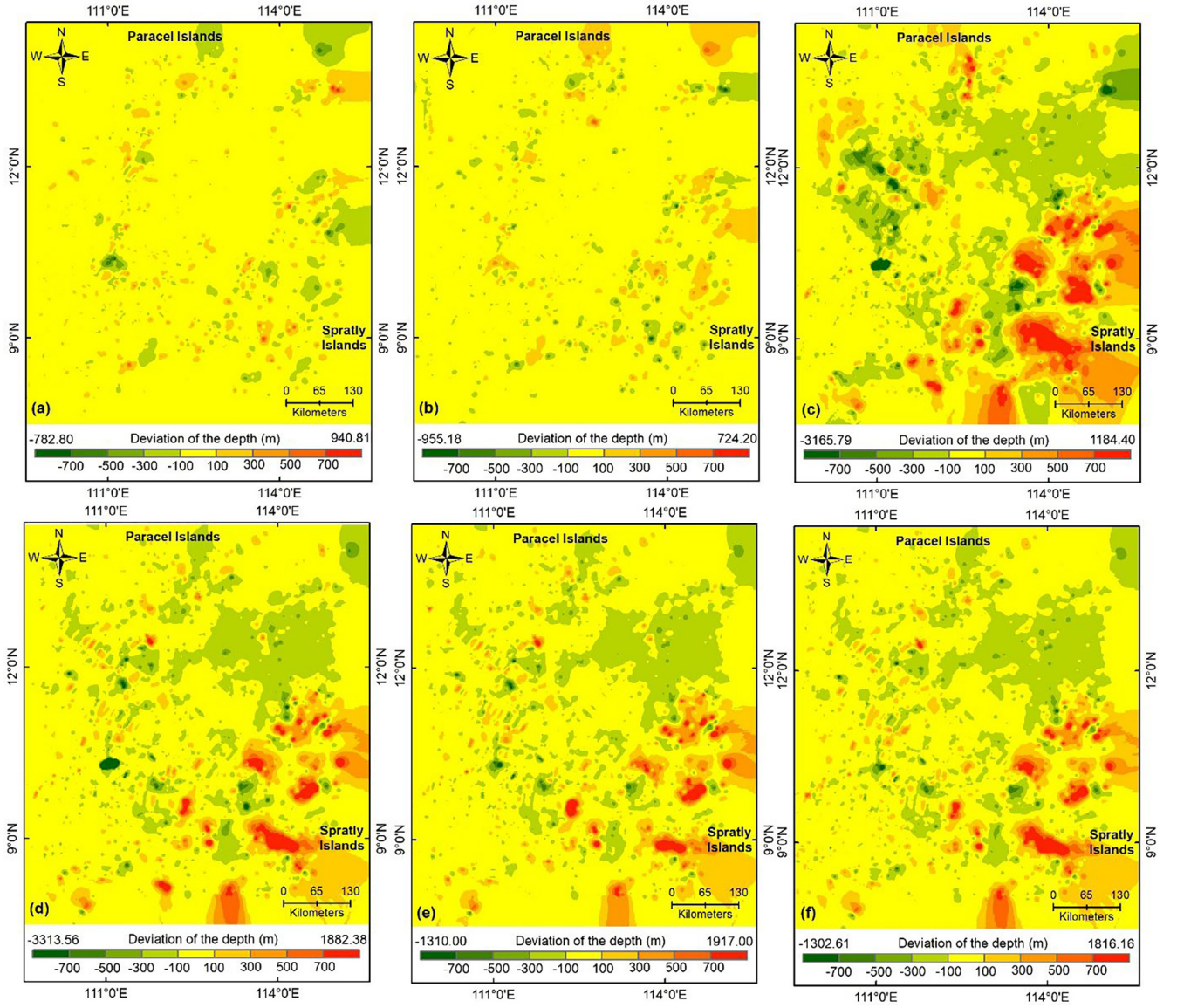
Fig. 13. Maps showing the difference between the shipborne depth data and six models: (a) the seafloor depth before the fitting depth; (b) the seafloor depth after the fitting depth (the final seafloor depth); (c) the DTU18BAT model; and (d) the GEBCO 2020 model, (e) the GEBCO 2022 model; and (f) the TOPO-V25.1 model.

result shows that the seafloor depth's Max, Min, Mean, and RMSD before and after the fitting depth are lower than that of the four global models, whereas r is higher (Table 7), indicating that the accuracy of the seafloor depth maps (before the fitting depth and after the fitting depth) is higher than those of the four global models in the study area.

The distribution of the difference between the shipborne depth data and six seafloor maps is shown in Fig. 13. It can be seen that the largest differences are in the Spratly Islands area, which is indicated by the red color in the map.

The correlation between the shipborne depth data and the six models is further illustrated in Fig. 14. It can be seen that the R^2 of the first two models (Fig. 14a and 14b) is 0.994, which is higher than that of the four global models, the DTU18BAT model ($R^2 = 0.964$), the GEBCO 2020

model ($R^2 = 0.971$), the GEBCO 2022 model ($R^2 = 0.981$), the TOPO-V25.1 model ($R^2 = 0.980$). These confirm that the accuracy of the seafloor depth maps (before the fitting and after the fitting) is better than those of the four global models.

5. Discussion

Because of the mean deviation (δg_{mean}) between the five models (DTU10GRAV, DTU13GRAV, DTU15GRAV, DTU17GRAV, and SDUST21GRAV) and shipborne gravity data (Table 2) larger than 2.63 mGal; it could be said that there are systematic errors existed in these models. Besides, the standard deviation ranges from ± 5.60 mGal to ± 5.90 mGal. Therefore, fitting the values of these mod-
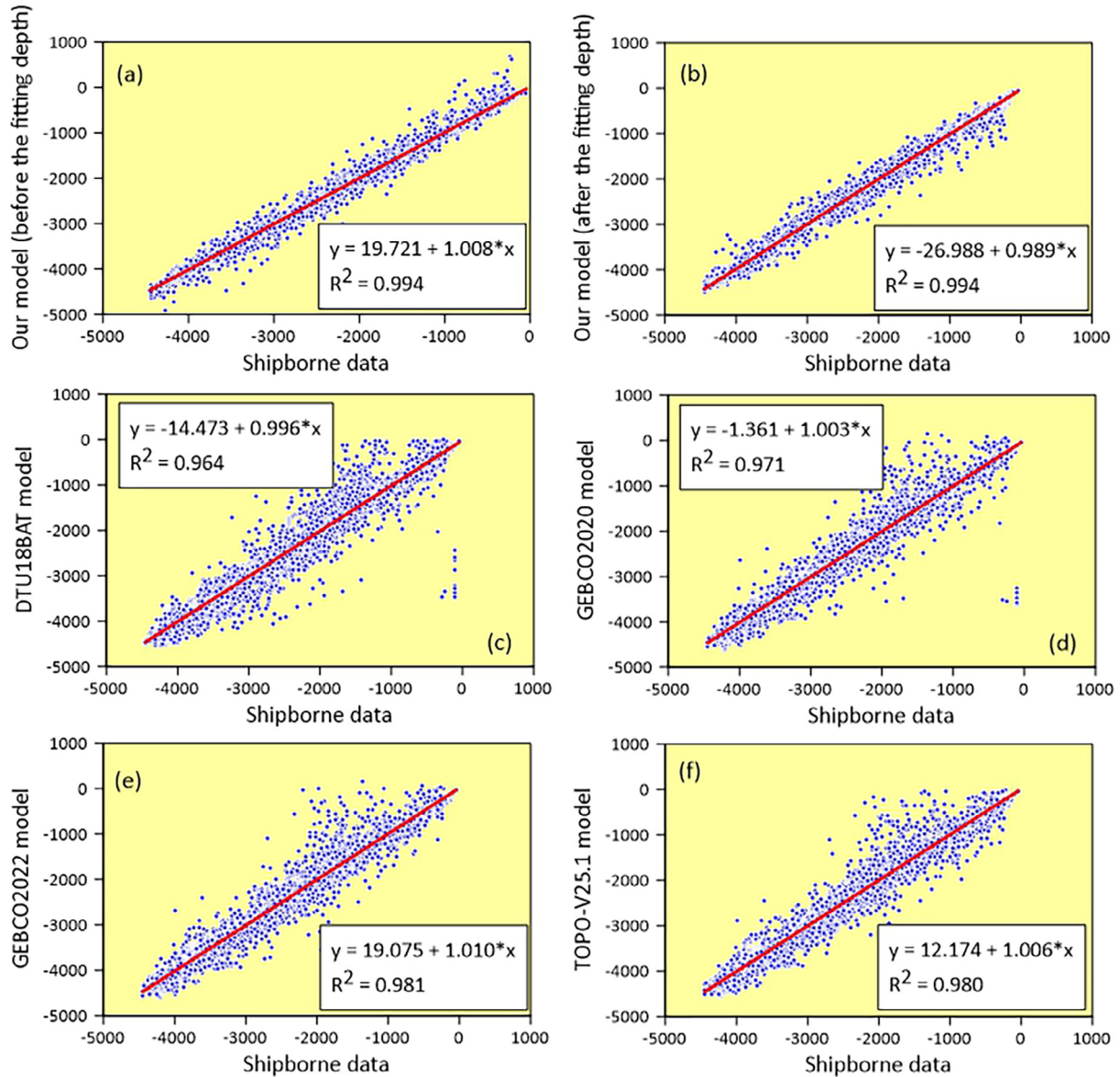
Fig. 14. The correlation between the shipborne depth data and the six models: (a) the seafloor depth before the fitting depth; (b) the seafloor depth after the fitting depth (the final seafloor depth); (c) the DTU18BAT model; and (d) the GEBCO 2020 model, (e) the GEBCO 2022 model; and (f) the TOPO-V25.1 model.

els with shipborne gravity data is necessary, which helps to eliminate that systematic errors and improve accuracy.

The result of this research demonstrates that the Collocation method (Neiman, 2010b) is a good solution for reducing the systematic errors above and improving the accuracy. Thus, the MD and RMSD of the satellite-derived gravity anomaly before the fitting are 4.98 mGal and ± 7.25 mGal, respectively, corresponding to 33.12 m (MD) and ± 119.74 m (RMSD) of our computed gravity-derived depth. However, after the fitting gravity anomaly, the MD and RMSD values reduced to 0.28 mGal and ± 5.05 mGal, respectively. These correspond to −1.18 m (MD) and ± 85,536 m (RMSD) of the gravity-derived seafloor depth.

In other words, in this research, an error of ± 1.0 mGal in the gravity anomaly leads to an error of ± 17.0 m in the depth measurement, with the SDC is 1.40 g/cm^3. Thus, to increase the accuracy of the gravity depth determination, it is necessary to improve the satellite-derived gravity anomaly. Thus, the use of combined data from recent new satellite generations (i.e., SARAL/AltiKa and Sentinel-6) and the old satellite generations (i.e., Jason 1, 2, and Cyosat-2) is the suitable solution.

The accuracy of the gravity depth result is also strongly influenced by the SDC; therefore, it is essential to determine the SDC properly. The finding of this work denotes that the iteration process is the suitable method to determine the SDC. Besides, the shipborne measurement is

expensive and time-consuming; therefore, combining the satellite-derived gravity data and shipborne measured data can reduce the workload of the direct measurement.

Finally, although the GEBCO 2022 provides the seafloor depth with the highest accuracy (RMSD = ±152.88 m) for the study area compared to those of DTU18BAT, GEBCO 2020, and TOPO-V25.1; however, the accuracy is still lower than that from our result (RMSD = ±83.96 m). This is because the seafloor topography of the study area is complex, with different coral reefs and sinking islands that are difficult to estimate the depth from gravity. Thus, the inclusion of shipborne data plays a critical role in the improvement of depth accuracy.

6. Conclusion

This study explores the possibility of improving the accuracy of seafloor topographic mapping for a complex region of the central coast of Vietnam and its vicinity by using a combination of satellite-derived gravity anomaly and shipborne data. A seafloor topographic map with $1' \times 1'$ grid obtained by Gravity-Geology method. Based on the obtained results, some conclusions can be drawn as follows:

■ The selection of the gravity model for calculating the sea flood depth mapping plays an important role. Among the available gravity models, the DTU17GRAV model is capable of providing the best result.

■ The accuracy of the satellite-derived gravity anomaly is improved significantly by fitting the shipborne gravity anomaly data. The RMSD value of the DTU17GRAV reduces from RMSD ± 7.25 mGal to ± 5.06 mGal, and the MD decreases from + 4.98 mGal to + 0.28 mGal.

■ The iteration process is a suitable method to determine the SDC, and the appropriate SDC is 1.40 g/cm^3 for the study area.

■ Overall, the accuracy (RMSD) of the seafloor topographic map in this research is ± 83.96 m compared to the shipborne depth data. This RMSD is very much lower than that of GEBCO 2022, RMSD = ±152.88 m. Therefore, it is concluded that the combination of satellite-derived gravity anomaly and shipborne data can improve the accuracy of seafloor topographic mapping significantly.

Declaration of Competing Interest

The authors declare that they have no known competing financial interests or personal relationships that could have appeared to influence the work reported in this paper.

Appendix.

Nomenclature	Description
Δg^{alt}	Satellite-derived gravity anomaly
Δg^{ship}	Ship-derived gravity anomaly
Δg^{fit}	Fitted gravity anomaly
Δg^{long}	Long-wavelength gravity anomaly
Δg^{short}	Short-wavelength gravity anomaly
δg	Gravity anomaly deviation
δg_{mean}	Mean deviation of gravity anomaly
D^{ship}	Ship-derived depth
D^{grav}	Gravity-derived depth
D^{fit}	Fitting the gravity-derived seafloor depth and the shipborne depth
δD	Depth deviation
δD_{mean}	Mean deviation of depth
STD	Standard deviation
$RMSD$	Root mean square deviation

References

Abulaitijiang, A., Andersen, O.B., Sandwell, D.T., 2019. Improved Arctic Ocean bathymetry derived from DTU17 gravity model. Earth Space Sci. 6, 1336–1347. https://doi.org/10.1029/2018EA000502.

Adler, J., Parmryd, I., 2010. Quantifying colocalization by correlation: the Pearson correlation coefficient is superior to the Mander's overlap coefficient. Cytometry 77A, 733–742. https://doi.org/10.1002/cyto.a.20896.

An, D., Guo, J., Li, Z., Ji, B., Liu, X., Chang, X., 2022. Improved gravity-geologic method reliably removing the long-wavelength gravity effect of regional seafloor topography: a case of bathymetric prediction in the South China Sea. IEEE Trans. Geosci. Remote Sens. 60, 1–12. https://doi.org/10.1109/TGRS.2022.3223047.

Andersen, O.B., Knudsen, P., 2014. Global and Arctic Marine Gravity Field From Recent Satellite Altimetry (DTU13). In: 76th EAGE Conference and Exhibition. European Association of Geoscientists & Engineers, pp. 1–5. https://doi.org/10.3997/2214-4609.20140897.

Andersen, O.B., Knudsen, P., 2016. Deriving the DTU15 Global high resolution marine gravity field from satellite altimetry. ESA Living Planet Symposium 2016. Prague, Czech Republic.

Andersen, O.B., Knudsen, P., 2020. The DTU17 Global Marine Gravity Field: First Validation Results. In: Mertikas, S.P., Pail, R. (Eds.), Fiducial Reference Measurements for Altimetry. Springer, International Association of Geodesy Symposia, pp. 83–87. https://doi.org/10.1007/1345_2019_65.

Andersen, O.B. Marine Gravity and Geoid from Satellite Altimetry. Geodetic Department, DTU - Space, Juliane Maries Vej 30, DK - 2100, Denmark., pp. 401-51, 2013. https://doi.org/10.1007/978-3-540-74700-0_9.

Arnould, J.P., Monk, J., Ierodiaconou, D., et al., 2015. Use of anthropogenic sea floor structures by Australian fur seals: potential positive ecological impacts of marine industrial development? PLoS One 10, e0130581.

Arseni, M., Voiculescu, M., Georgescu, L.P., Iticescu, C., Rosu, A., 2019. Testing different interpolation methods based on single beam echosounder river surveying. case study: Siret River. Int. J. Geo-Informat. 8. https://doi.org/10.3390/ijgi8110507.

Becker, J.J., Sandwell, D.T., Smith, W.H.F., Braud, J., Binder, B., Depner, J., 2009. Global bathymetry and elevation data at 30 arc seconds resolution: SRTM30_PLUS. Mar. Geod. 32, 355–371. https://doi.org/10.1080/01490410903297766.

Brêda, J.P.L.F., Paiva, R.C.D., Bravo, J.M., Passaia, O.A., Moreira, D.M., 2019. Assimilation of satellite altimetry data for effective river bathymetry. Water Resour. Res. 55, 7441–7463. https://doi.org/10.1029/2018WR024010.

Bui, C.Q., Tran, T.D. Building an atlas of basic characteristics of natural and environmental conditions in Vietnam and adjacent waters. State-level project KC-09-02, Marine Research Program. Hanoi, Vietnam, 2005

Calder, B.R., Mayer, L.A., 2003. Automatic processing of high-rate, high-density multibeam echosounder data. Geochem. Geophys. Geosyst. 4. https://doi.org/10.1029/2002GC000486.

Cohen, F.E., Sternberg, M.J.E., 1980. On the prediction of protein structure: the significance of the root-mean-square deviation. J. Mol. Biol. 138, 321–333. https://doi.org/10.1016/0022-2836(80)90289-2.

Costa, B., Battista, T., Pittman, S., 2009. Comparative evaluation of airborne LiDAR and ship-based multibeam SoNAR bathymetry and intensity for mapping coral reef ecosystems. Remote Sens. Environ. 113, 1082–1100. https://doi.org/10.1016/j.rse.2009.01.015.

Crosby, A.G., McKenzie, D., Sclater, J.G., 2006. The relationship between depth, age and gravity in the oceans. Geophys. J. Int. 553–73, 2006. https://doi.org/10.1111/j.1365-246X.2006.03015.x.

Dixon, T.H., McNutt, M.K., Smith, S.M., 1983. Bathymetric prediction from SEASAT altimeter. J. Geophys. Res. Solid Earth 88, 1563–1571. https://doi.org/10.1029/JC088iC03p01563.

Forsberg, R., 1987. A new covariance model for inertial gravimetry and gradiometry. J. Geophys. Res. Solid Earth 92, 1305–1310. https://doi.org/10.1029/JB092iB02p01305.

Forsberg, R., Tscherning, C.C., 2008. An overview manual for the GRAVSOFT geodetic gravity field modelling programs. DTU Space.

GEBCO Bathymetric Compilation Group. The GEBCO_2020 Grid - a continuous terrain model of the global oceans and land. . British Oceanographic Data Centre, National Oceanography Centre, NERC, UK, 2020. https://doi.org/10.5285/a29c5465-b138-234d-e053-6c86abc040b9.

GEBCO Bathymetric Compilation Group. The GEBCO_2022 Grid - a continuous terrain model of the global oceans and land. NERC EDS British Oceanographic Data Centre NOC, 2022. https://doi.org/10.5285/e0f0bb80-ab44-2739-e053-6c86abc0289c

Gonzalez, N.M., Waldman, R., Sannino, G., Giordani, H., Somot, S., 2023. Understanding tidal mixing at the Strait of Gibraltar: a high-resolution model approach. Prog. Oceanogr. 212. https://doi.org/10.1016/j.pocean.2023.102980 102980.

Haxby, W.F., Karner, G.D., LaBrecque, J.L., Weissel, J.K., 1983. Digital images of combined oceanic and continental data sets and their use in tectonic studies. Trans. Am. Geophys. Union 64, 995–1004. https://doi.org/10.1029/EO064i052p00995.

Hildebrand, L.P., Bellefontaine, N.A., 2017. Ocean Governance and sustainability. Ship. Oper. Manag. 231–48. https://doi.org/10.1007/978-3-319-62365-8_11.

Ibrahim, A., Hinze, W.J., 1972. Mapping buried bedrock topography with gravity. Groundwater 10, 18–23. https://doi.org/10.1111/j.1745-6584.1972.tb02921.x.

IHO, IOC. The IHO-IOC GEBCO Cook Book. International Hydrographic Organization, Intergovernmental Oceanographic Commission (IHO-IOC), Monaco, 2018. http://dx.doi.org/10.25607/OBP-709.

Jakobsson, M., Mayer, L., Armstrong, A., 2003. Analysis of data relevant to establishing outer limits of a continental shelf under law of the sea. Int. Hydrogr. Rev. 4, 1–18 https://journals.lib.unb.ca/index.php/ihr/article/view/20602/23764.

Kaiser, M.J., 2020. The Offshore Pipeline Construction Industry: Activity Modeling and Cost Estimation in the US Gulf of Mexico. Gulf Professional Publishing.

Kim, K.B., Hsiao, Y.-S., Kim, J.W., Lee, B.Y., Kwon, Y.K., Kim, C.H., 2010. Bathymetry enhancement by altimetry-derived gravity anomalies in the East Sea (Sea of Japan). Mar. Geophys. Res. 31, 285–298. https://doi.org/10.1007/s11001-010-9110-0.

Knudsen, P., Andersen, O.B., Forsberg, R., Roberto, S., Henning, S. Satellite bathymetry and other satellite derived data. National Space Institute, DTU-SPACE, 2012

Kostoglodov, V., Kogan, M., Magnitskaya, E., 1981. Isostasy of the southern Mid-Atlantic Ridge: long-wavelength and short-wavelength effects. J. Geophys. Res. Solid Earth 86, 7825–7841. https://doi.org/10.1029/JB086iB09p07825.

Kruss, A., Wiktor, J., Tatarek, A. Acoustic detection of macroalgae in a dynamic Arctic environment (Isfjorden, West Spitsbergen) using multibeam echosounder. 2019 IEEE Underwater Technology (UT). IEEE, pp. 1-7, 2019. https://doi.org/10.1109/UT.2019.8734323.

Kwang, B.K., Yu-Shen, H., Jeong, W.K., Bang, Y.L., Yi, K.K., Chang, H.K., 2010. Bathymetry enhancement by altimetry-derived gravity anomalies in the East Sea (Sea of Japan). Mar. Geophys. Res. 285–98, 2010. https://doi.org/10.1007/s11001-010-9110-0.

Liu, H., Sherman, D., Gu, S., 2007. Automated extraction of shorelines from airborne light detection and ranging data and accuracy assessment based on Monte Carlo simulation. J. Coast. Res. 23, 1359–1369. https://doi.org/10.2112/05-0580.1.

Lucieer, V.L., Forrest, A.L., 2016. Emerging Mapping Techniques for Autonomous Underwater Vehicles (AUVs). In: Finkl, W.C., Makowski, C. (Eds.), Seafloor Mapping Along Continental Shelves: Research and Techniques for Visualizing Benthic Environments. Springer International Publishing, p. 14. https://doi.org/10.1007/978-3-319-25121-9_2.

Mathez, E., Smerdon, J. Greenland, Antarctica, and Sea-Level Rise. Climate Change. Columbia University Press, 305-30, 2018. https://doi.org/10.7312/math17282-012

Neiman, Y.M., 2010. Covariance method in physical geodesy and collocation. Moscow Scientific World, Moscow, Russia.

Nguyen, V.S., 2013. Fitting the satellite-derived gravity anomaly with the ship-derived gravity anomaly. Scient. Tech. J. Mining – Geol. 44, 44–48.

Nguyen, T.T. Study of geological structure in deep sea (over 200m water) South Vietnam as a scientific basis for searching related mineral resources. Final report on topic KC09.18/06-10., 2010.

Nguyen, V.S. Determination of gravity anomalies for Vietnamese waters by satellite altimeter results. Moscow State University of Geodesy and Cartography, Russian Federation, pp. 160, 2012

Pe'eri, S., Parrish, C., Azuike, C., Alexander, L., Armstrong, A. Satellite remote sensing as a reconnaissance tool for assessing nautical chart adequacy and completeness. Marine Geodesy 37, 293-314, 2014. https://doi.org/10.1080/01490419.2014.902880

Phillips, R.J., Lambeck, K., 1980. Gravity fields of the terrestrial planets: long-wavelength anomalies and tectonics. Rev. Geophys. 18, 27–76. https://doi.org/10.1029/RG018i001p00027.

Que, B.C., Dung, T.T., Tram, L., 2008. Construction of bouguer gravity anomaly map in the Vietnam Sea and adjacent area. Vietnam J. Mar. Sci. Technol. 8. https://doi.org/10.15625/1859-3097/6298.

Sagawa, T., Yamashita, Y., Okumura, T., Yamanokuchi, T., 2019. Satellite derived bathymetry using machine learning and multi-temporal satellite images. Remote Sens. (Basel) 11. https://doi.org/10.3390/rs11101155.

Sepúlveda, I., Liu, P.-L.-F., Grigoriu, M.D., 2018. Probabilistic tsunami hazard assessment in South China Sea with consideration of uncertain earthquake characteristics. J. Geophys. Res. Solid Earth 124, 658–688. https://doi.org/10.1029/2018JB016620.

Smith, W.H.F., Sandwell, D.T., 1994. Bathymetric prediction from dense satellite altimetry and sparse shipboard bathymetry. J. Geophys. Res. 99, 21803–21824. https://doi.org/10.1029/94JB00988.

Smith, W.H.F., Sandwell, D.T., 1997. Global sea floor topography from satellite altimetry and ship depth soundings. Science 277, 1956–1962. https://doi.org/10.1126/science.277.5334.1956.

Sun, Z., Ouyang, M., Guan, B., 2018. Bathymetry predicting using the altimetry gravity anomalies in South China Sea. Geod. Geodyn. 9, 156–161. https://doi.org/10.1016/j.geog.2017.07.003.

Thomas, N., Lee, B., Coutts, O., Bunting, P., Lagomasino, D., Fatoyinbo, L., 2022. A purely spaceborne open source approach for regional bathymetry mapping. IEEE Trans. Geosci. Remote Sens. 60, 1–9. https://doi.org/10.1109/TGRS.2022.3192825.

Tozer, B., Sandwell, D.T., Smith, W.H.F., Olson, C., Beale, J.R., Wessel, P., 2019. Global bathymetry and topography at 15 arc sec: SRTM15+. Earth Space Sci. 6, 1847–1864. https://doi.org/10.1029/2019EA000658.

Traganos, D., Poursanidis, D., Aggarwal, B., Chrysoulakis, N., Reinartz, P., 2018. Estimating Satellite-Derived Bathymetry (SDB) with the google earth engine and Sentinel-2. Remote Sens. (Basel) 10, 859. https://doi.org/10.3390/rs10060859.

VNHOD. Report on the results of the project: Measuring and mapping the sea in the Spratly Islands area, DK1 scale 1:200000; 1:50000.

Vietnam's People Naval Hydrographic and Oceanographic Department, 2000

Wei, Z., Guo, J., Zhu, C., Yuan, J., Chang, X., Ji, B., 2021. Evaluating accuracy of HY-2A/GM-derived gravity data with the gravity-geologic method to predict bathymetry. Front. Earth Sci. 9. https://doi.org/10.3389/feart.2021.636246.

Wölfl, A.-C., Snaith, H., Amirebrahimi, S., et al., 2019. Seafloor mapping–the challenge of a truly global ocean bathymetry. Front. Mar. Sci. 283. https://doi.org/10.3389/fmars.2019.00283.

Xiang, X., Wan, X., Zhang, R., Li, Y., Sui, X., Wang, W., 2017. Bathymetry inversion with the gravity-geologic method: a study of long-wavelength gravity modeling based on adaptive mesh. Mar. Geod. 40, 329–340. https://doi.org/10.1080/01490419.2017.1335257.

Xueshuang, X., Xiaoyun, W., Running, Z., Yang, L., Xiaohong, S., Wenbin, W., 2017. Bathymetry inversion with gravity-geologic method: a study of long-wavelength gravity modeling based on adaptive mesh. Mar. Geod. https://doi.org/10.1080/01490419.2017.1335257.

Yeu, Y., Yee, J.-J., Yun, H.S., Kim, K.B., 2018. Evaluation of the accuracy of bathymetry on the nearshore coastlines of Western Korea from satellite altimetry, multi-beam, and airborne bathymetric LiDAR. Sensors 18. https://doi.org/10.3390/s18092926.

Yu-Shen, H., Jeong, W.K., Kwang, B.K., Bang, Y.L., Cheinway, H., 2010. Bathymetry estimation using the gravity-geologic method: an investigation of density contrast predicted by the downward continuation method. Terr. Atmos. Ocean. Sci. 22, 347–358. https://doi.org/10.3319/TAO.2010.10.13.01(OC).

Zhu, C., Guo, J., Yuan, J., Li, Z., Liu, X., Gao, J., 2022. SDUST2021-GRA: global marine gravity anomaly model recovered from Ka-band and Ku-band satellite altimeter data. Earth Syst. Sci. Data 14, 4589–4606. https://doi.org/10.5194/essd-14-4589-2022.